POLITECNICO
MILANO 1863

SCUOLA DI INGEGNERIA INDUSTRIALE
E DELL'INFORMAZIONE

Executive Summary of the Thesis

A Scientific Study on Remote Sensing of Forest Areas by Synthetic Aperture Radar Tomography in the context of TomoSense Experiment

Laurea Magistrale in Space Engineering - Ingegneria Spaziale

Author: Marco di Trocchio

Advisor: Prof. Stefano Tebaldini

Co-advisor: Mauro Mariotti d'Alessandro

Academic year: 2021-2022

Abstract

Satellite imagery and secondary products play a relevant role in supplying the information necessary for analysing, monitoring and characterising Earth's Forest globally in a short time interval and, in this perspective, low band Synthetic Aperture Radar (SAR) Tomography (TomoSAR) is one of the most promising technology.This thesis is intended to provide a preliminary evaluation on the potentiality of P- and L-band SAR Tomography to be related to the biophysical properties of natural media in a scientific study supported by real data acquired in the context of TomoSense experiment that comprises a series of aerial and terrestrial campaigns over the Eifel National Park, in Germany in support of the future European Space Agency Earth Explore Mission BIOMASS. The first part focuses on assessing a qualitative comparison between the 3D TomoSAR produced by coherently combing stack of SAR images, referred to as coherent tomography, and by processing multiple simultaneous single-pass acquisitions in the so-called correlation tomography. A second part propose a method for the retrieval of the canopy top-height based on 3D TomoSAR reflectivity profiles. Finally the analysis focuses on assessing the correlation between TomoSAR and the biophysical properties of forest by proposing a comparison between deciduous and coniferous forests.

Keywords: Synthetic Aperture Radar (SAR) Tomography (TomoSAR); Remote Sensing; Forestry; Above Ground Biomass; Canopy Height; BIOMASS; Eifel National Park; Bistatic Radar

1. Introduction

Climate change is a challenging problem that has major impacts on human and natural ecosystems and forests play a relevant role in the global carbon cycle, and subsequently in the global climate [1; 2]. However, due to the practical difficulties in monitoring forest globally, one of the greatest uncertainties affecting the global carbon budget arises from the lack of information on forests biophysical properties. In the last decades space agencies has invested in research activities based on airborne or satellite systems to assess the potentials of SAR tomography in the context of forestry remote sensing [3–6]. European Space Agency (ESA) organised a series of research and experimental campaigns in support of the next Earth Explorer Mission BIOMASS [7] including TomoSense experiment [8], carried out between 2019 and 2021 at the Eifel National Park, in Germany, whose data will be analysed in the frame of this work. TomoSense dataset comprises a fully polarimetric SAR surveys at P- and L-band by flying simultaneously two aircraft to provide monostatic and bistatic SAR acquisition, completed by a detailed forest census of more than +2600 trees, Terres-

trial Laser Scanning (TLS), Airborne Laser Scanning (ALS) and an estimated AGB model. The blended knowledge about the test site offers the opportunity to investigate the synergies between P- and L-band in forestry application in support of bistatic SAR mission as in the case of Tandem-L [9] , or SAOCOM-CS [10].
This paper attempts to summarise the relevant analysis in the context of the thesis as a demonstration of the potentials of future scientific research on TomoSAR applications.
First, the principles of TomoSAR will be illustrated by proposing a comparison between classical 3D focusing of the stack of 2D SAR images, the so called coherent tomography, and TomoSAR processing from multiple stack of simultaneous single-pass acquisition, known as correlation tomography. Then, according to the penetration capability exhibits by low band SAR Tomography, an algorithm for the estimation and retrieval of the canopy top height is proposed both in the case of P- and L-band. Finally the analysis focuses on the evaluation of possible relation between TomoSAR vertical profiles and biophysical properties of a temperate forest.

2. Test Site

The area of study comprises a portion of the Kermeter Forest, located in the Eifel National Park in the North Rhine-Westphalia region, in Germany (50° 35' 15.7" N, 6° 29' 41.7" E), shown in an aerial picture in Fig. 1.

Figure 1: Kermeter Forest in the Eifel National Park, North Rhine-Westphalia, Germany

The proposed Region Of Interest (ROI), in the context of TomoSense Experiment, comprises an area of about ∼2726,75 hectares.
According to German forestry classification (Fig. 2), the area is mostly dominated by beech woods and a consistent percentage of spruces which belongs respectively to the class of deciduous and coniferous trees. Deciduous refers typically to broadleaf trees that loose all their leaves during the coldest period of the year and they tend to grow outward to optimise light absorbance (Fig. 3a), while coniferous are often referred to as evergreens because they have leaves in

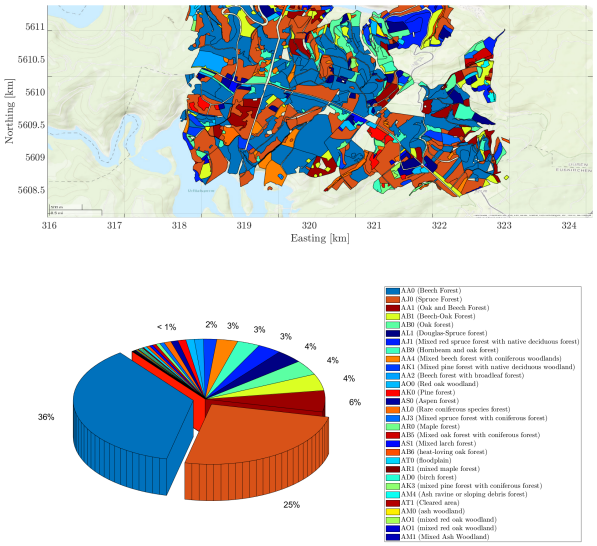

Figure 2: Forest Classification of the ROI in the Kermeter Forest, Germany

all seasons and are characterised by a conical shape (Fig. 3b).

(a) Kermeter Beeches, Deciduous Trees

(b) Kermeter Spruces, Conifer Trees

Figure 3: Terrestrial and Aerial Photography of Deciduous and Conifer trees in the Efiel National Park

In Kermeter forests, conifer and deciduous vegetations may exhibit different feature in radiation scattering of leaves vs. needles, along with typically round (deciduous) vs. conical (conifer) shapes, and the vertical distribution of foliage within the canopy.

2.1. Field Campaign

A field campaign has been conducted in the Kermeter Area in spring 2019 by the Research Department of Eifel National Park Administration. A total of about +2600 trees within 80 plots that cover an area of about 6.25 hectares each and spaced by 250x250 m^2 were measured. The objective was to provide a tree census that collects several tree including trees GPS position, species, status (living, death or dying), height, diameter, etc..

2.2. Airborne Laser Scanning (ALS)

TomoSense dataset is supported by small-footprint Airborne Laser Scanning measurement over the test site acquired by CzechGlobe in July 2018 and then complemented with an additional campaign in 2021 in the context of the ESA campaign FLEXSense [11]. The derived products include terrain topography, Canopy Height Model (CHM) and Above Ground Biomass estimation model. LiDAR derived canopy height and AGB model estimates in 2022

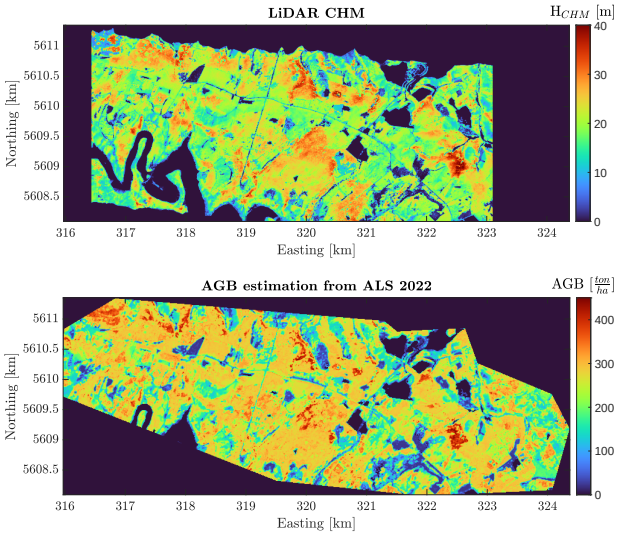

Figure 4: LiDAR Canopy Height Model (up) and Above Ground Biomass (bottom) by CzechGlobe

2.3. Synthetic Aperture Radar (SAR) campaigns

A series of airborne SAR campaigns were carried out by MetaSensing between July and November 2020. The acquired data comprises fully polarimetric SAR surveys at P- and L-band by flying simultaneously two aircraft about 25 times (20 in the case of P-band and 30 in L-band) with multiple baselines in two opposite look direction which we referred to as North-West (NW) and South-East (SE) looks, to provide monostatic and bistatic SAR imaging capabilities. All the results obtained in the context of this thesis are supported by SAR images properly coregistered by Politecnico di Milano department [12].

3. TomoSAR processing

TomoSAR processing is a straightforward extension of conventional SAR focusing from the 2D to the 3D domain. If more tracks are added to form multi-baselines (MB) almost parallel to each other a new aperture in the radar cross-range direction can be synthesised, resulting in 3D resolution capabilities. Considering N stack of SLC SAR images acquired along parallel trajectories, I_n(gr, x) represents the complex valued pixel at ground range, azimuth location (gr, x) in the *n-th* image and compensating the phase term associated to the ground [13], I_n can be expressed for each pixel as:

$$I_n = \int_C s(z, t_n) \cdot \exp\left(-j\frac{4\pi}{\lambda}\frac{b_n}{R_M(ref)}z\right)dz \quad (1)$$

where b_n is the normal baseline relative to the *nth* image with respect to a common master; λ is the carrier wavelength; z is the vertical coordinate derived from the projection of the cross-range coordinate de-

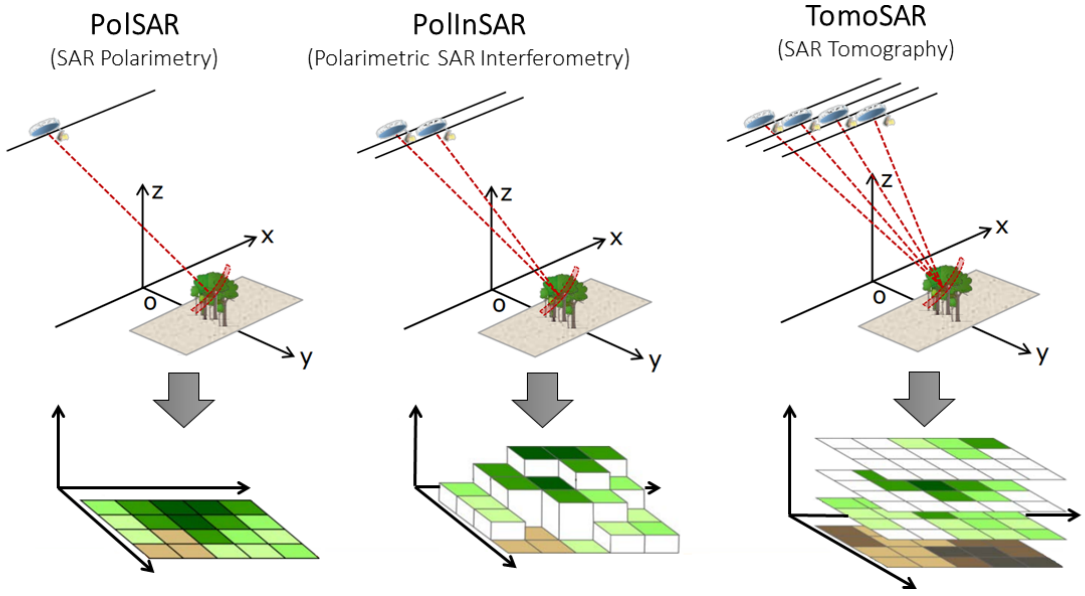

Figure 5: General scheme on the geometry of classical PolSAR, PolInSAR and TomoSAR. Credit: EO College

fined as orthogonal direction to the Radar Line-of-Sight (LOS); $s(z, t_n)$ is the average complex reflectivity within the slant range, azimuth, cross range voxels and t_n is the time of the *n-th* pass.

3.1. Coherent Tomography

Coherent tomography rely on the assumption that target reflectivity does not decorrelate over time **??**, meaning that: $s(z, t_n) \cong s(z)$. Therefore, by substituting the following to Eq. (1), it can be noticed that SAR data and target projections form a Fourier Pair. Thus, the complex reflectivity can be retrieved as the Discrete Fourier Transform (DFT) of the SLC SAR images:

$$\hat{s}(z) = \mathrm{DFT}\{I_n\} = \sum_{n=1}^{N} I_n \exp(jK_n z) \qquad (2)$$

where $K_n = n\Delta K = n\frac{4\pi}{\lambda}\frac{b_n}{R_M(ref)}$ defines the n-th elevation wavenumbers and N the number of tracks. By performing the 3D spatial multi-looking it is possible to retrieve the vertical backscatter intensity that will denotes the typical output of coherent tomography:

$$\hat{T}_{coh}(z) = \sum_{nm} \langle I_n \cdot I_m^* \rangle_L \exp(-j(K_n - K_m)z) \qquad (3)$$

where $\langle \boldsymbol{I_n} \cdot \boldsymbol{I_m^*} \rangle_L$ denotes the correlation between the n-th *master* and m-th *slave* acquisitions resulting from the spatial averaging of L range/azimuth look. Eq. (3) in large part of the literature is rearranged in a matrix notation as function of the interferometric coherences as:

$$\hat{T}_{coh}(z) = \boldsymbol{a}^T(z)\hat{\boldsymbol{R}}\boldsymbol{a}(z) \qquad (4)$$

where $\boldsymbol{a}(z_i) \in C^{N\mathrm{x}1}$ is the so-called steering vector containing the interferometric phase information and $\hat{\boldsymbol{R}} \in C^{N\mathrm{x}N}$ defines the full-ranked estimated coherence matrix for each pixel associated to all the possible baselines, positive defined by construction.

$$\boldsymbol{a}(z) = \begin{bmatrix} 1 & \exp(-jk_{z_2}z) & \cdots & \exp(-jk_{z_N}z) \end{bmatrix}^T$$

$$\hat{\mathbf{R}} = \begin{bmatrix} 1 & \gamma_{12} & \cdots & \gamma_{1N} \\ \gamma_{21} & 1 & & \\ \vdots & & \ddots & \vdots \\ \gamma_{N1} & & \cdots & 1 \end{bmatrix}$$

3.2. Correlation Tomography

In the case of repeat-pass SAR mission, the scene decorrelates over time due to time lags between acquisitions in the order of days, so that the randomly movement and oscillation of the vegetation results in changes in the speckle pattern, thus limiting the adoption of coherent tomography. A possible way to overcome this limitation is provided by bistatic SAR systems where the the acquired interferometric pairs result to be highly correlated since same targets are acquired almost simultaneously. According to that, the problem can be reformulated considering only N consecutive number of bistatic passes as illustrated in Fig. 6. This approach is called *correlation tomography* and it is based on the fundamental assumption the target reflectivity is *stationary* [14], which valid, in forest sites, until large structural variation on the vegetation occurs (e.g. seasonal variations, weather conditions, deforesting etc.. [15]).

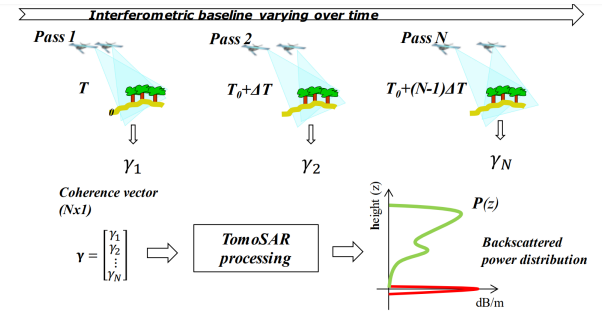

Figure 6: Typical scheme of single-pass InSAR image pairs for correlation tomography

Based on this, targets are allowed to decorrelate over time, while their statistical properties are assumed not dependent on acquisition time. Consider now a generic bistatic system, and let $gam\hat{m}a_n$ denotes the interferometric coherences between the n-th simultaneous acquisition, Eqs. (3) and (4) can be defined, in the case of correlation tomography, as:

$$\hat{T}_{cor}(z) = 1 + 2\mathrm{Re}\left(\sum_1^N \left(\frac{N+1-n}{N+1}\right)\hat{\gamma}_n \exp(-jK_n z)\right) \qquad (5)$$

3.3. Experimental Results

The case study here reported is relative to the airborne SLC SAR images at L-band acquired over the Eifel National Park. SAR Tomography has be derived from the real data coherence matrix $\hat{\boldsymbol{R}}$ in the frame of a classical problem of spectral estimation using the classical Fourier beamforming technique and using a sliding windows of 15mx15m for spatial averaging. Coherent tomography has been derived in the case of monostatic and bistatic acquisition, whereas, correlation tomography has been affected by aircraft misalignment during the acquisition. To overcome low coherent single-pass acquisition TomoSAR processing has been derived by combining pairs of single-pass acquisitions plus five bistatic pairs to recover partially the loss of coherence due to SAR geometry.
TomoSAR has been obtain by varying the number of looks, but, for the sake of simplicity in this paper only the results related to the full stack of data will be presented. Fig. 7 presents TomoSAR vertical pro-

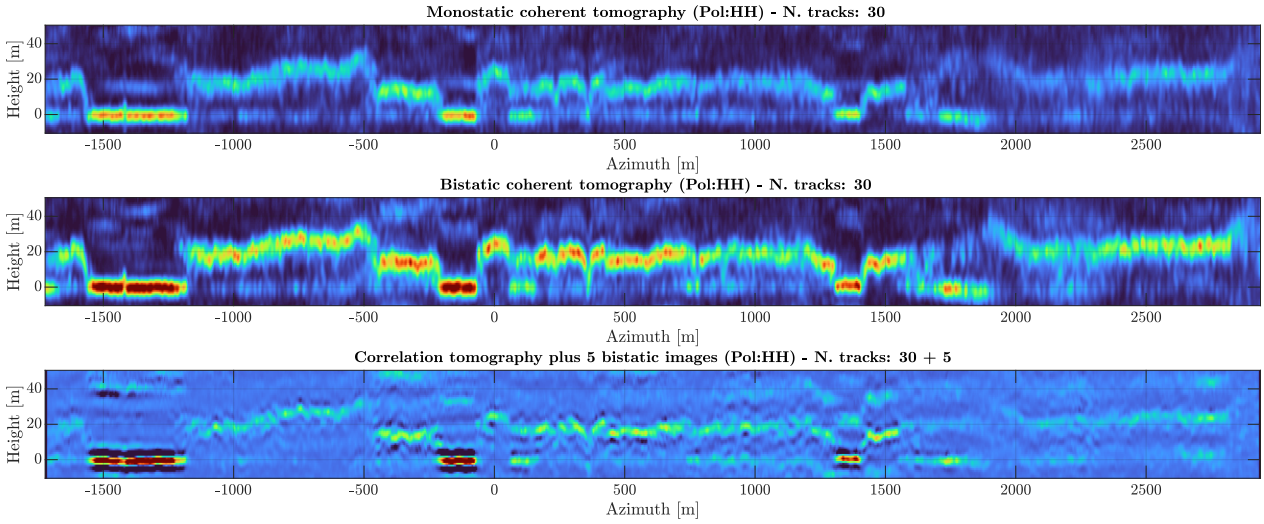

Figure 7: comparison beteen L-band airbone normalised Tomograms by coherent tomography of a stack of 30 monostatic images (up), bistatic images(center) and correlation tomography (bottom) recovered by the addition of 5 bistatic passes

file obtained in the frame of this work. The selected vertical slice is particularly interesting because of the presence of both grasslands and forested areas. The forest structure seems to be unveiled and imaging quality is fine enough to discriminate two distinct scattering layers, one associated to the ground and the other to the canopy by validating the results with LiDAR CHM. Bistatic coherent tomography shows stronger return in terms of backscatter intensity at the level of canopy with respect to the monostatic case, due to the geometry of the acquisition. Correlation tomography is not accurate as coherent, it is much prone to introduce artifacts and suffers of stronger oscillation with respect to the coherent TomoSAR, but the main feature of the forest are still visible demonstrating its capability to reconstruct the main feature of the vertical profile of a forest.
Therefore results confirm the high potentiality of correlation tomography as a valuable tool for future space mission with the advantage to rely on the processing of just 2N interferometric coherences with respect the N^2 required in case of coherent tomography, and to be non sensitive to targets decorrelation over time.

4. SAR Tomography in the Kermeter Forest

To investigate the relation between forests parameter (e.g. canopy height, biomass, etc..) and TomoSAR 3D backscatter intensities, TomoSAR cubes at P-band monostatic and L-band monostatic and bistatic were generated and geolocated with test site by Politecnico di Milano through Fourier beamforming of the full stack of data. TomoSAR has been normalised between 0 and N, maximum number of looks and the relative mean tomographic profiles are displayed in Fig. 8.

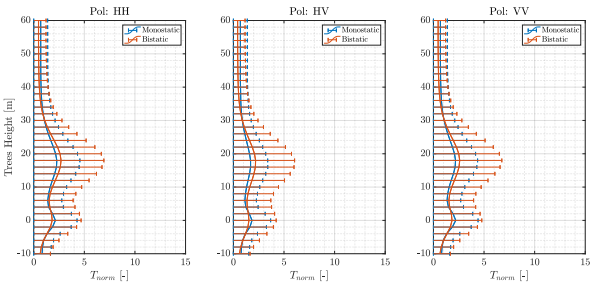

(a) L-band Monostatic and Bistatic

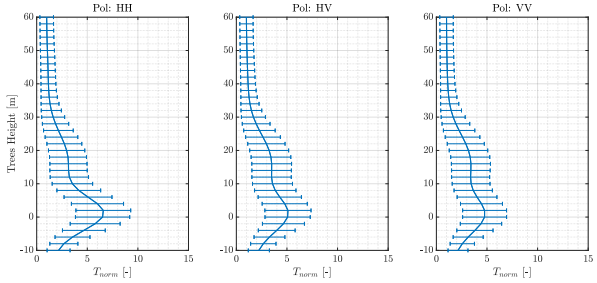

(b) P-band Monostatic

Figure 8: Normalised mean tomographic profiles associated to L-band (up) and P-band (bottom) TomoSAR in the Kermeter Area

Results revealed a striking difference in terms of the location of dominant back-scattering for the two wavelengths: at L-band the coherent backscattering from the canopy is visible in all polarization channels and it is particularly intense with respect to the ground scattering in the bistatic case, whereas, at P-band, it exhibits a local maximum at the canopy level with moderate in intensity. We conclude that at P-band the canopy forest under investigation is almost transparent to the microwaves which are mostly reflected at the level of trunk-ground, making it the most robust wavelength to forest changes, while, at L-band, both the forest canopy and ground are well detected and changes in the forest structure can bring changes in TomoSAR intensities.

4.1. Volume To Ground Ratio

Forests, from a TomoSAR point of view, can be seen as a two layers scatterers as noticed by looking at tomographic profiles. Thus, it is possible to evaluate the mutual interaction between them by defining the so-called Volume To Ground Ratio (RVoG). Volume to ground ratio is defined as the ratio between the backscatter power intensities associated to the canopy and the one associated to the ground. Both this parameter can be retrieved from the L-band and P-band tomographic cubes by considering:

- **Ground Power** (P_{ground}): integrating between $\pm$ 7 m around the dtm level
- **Canopy Power** (P_{canopy}): integrating between $\pm$ 7 m around the dtm level + CHM level

For each pixel in ground range and azimuth coordinate is then possible to evaluate the Volume To Ground ratio as:

$$RVoG(pol) = 10log_{10}\left(\frac{P_{canopy}(pol)}{P_{ground}(pol)}\right) \quad (6)$$

The relative maps associated to P- and L-band are displayed in Fig. 9 This parameter express the relative contribution of canopy with respect to the ground. Positive values in the map (brighter areas in the map) indicates areas where the contribution of canopy is stronger with respect to the ground while negative areas (darker areas in the map) typically indicates grasslands. This coefficient will be useful further to investigate the correlation between TomoSAR and forests properties.

5. Canopy Height Retrieval

Estimating forest top height is a challenging task because it is often hard to clearly identify the top leaf or branch of trees in the canopy. Due to its ability to accurately characterize the vertical profile of forests, TomoSAR can be used to estimate the canopy top height. Forest vertical structure can be observed by analysing the tomographic profiles at each pixel location. The reflectivity profiles will be characterised

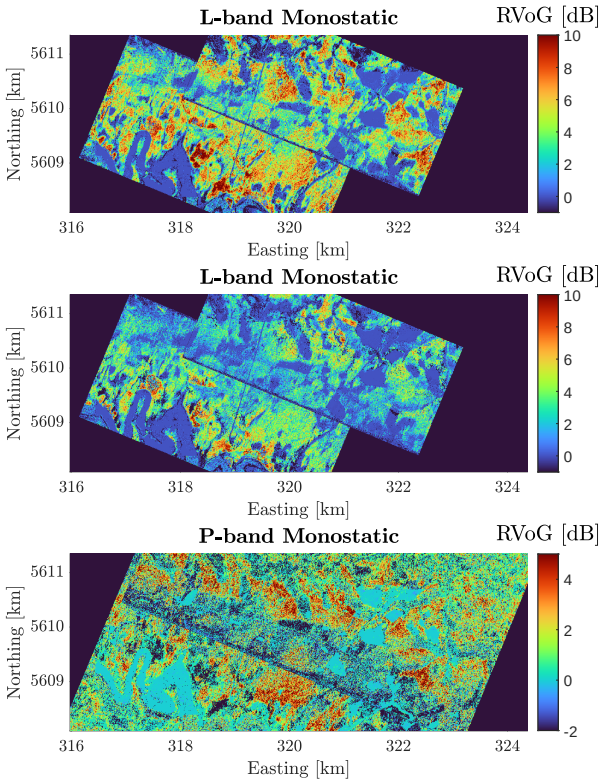

Figure 9: Volume To Ground Ratio Associated to L-band bistatic (top), monostatic (center) and P-band monostatic (bottom) for VV polarimetric channel

by a certain number of peaks and an effective phase center H_C, where most of the backscatter is concentrated and can be retrieved by TomoSAR as:

$$H_C(gr, x) = argmax\left(T(gr, x, z)\right) \quad (7)$$

where T(z, r, x) is the vertical backscatter at ground range, azimuth location in vertical direction z.
The phase center has not to be confused with the top-of-canopy height because of the penetration capability of low frequency band. Thus, the canopy top height can be retrieved by evaluating the power loss from the phase center location in the upper envelope [16; 17], as:

$$\hat{H}(gr, x) = argmin(T(gr, x, z) - T(gr, x, H_C) - K) \quad (8)$$

where T(gr,x,z) is the backscatter vertical profile, H_C is the elevation of the phase center and K is the power loss factor. The canopy top height retrieval depends on the choice of the K value, we used the CHM from the airborne SAR dataset to select the optimal height by comparing the estimated model and the LiDAR CHM measurements.

The resulting map of the retrieved phase center height is shown in Fig. 10.

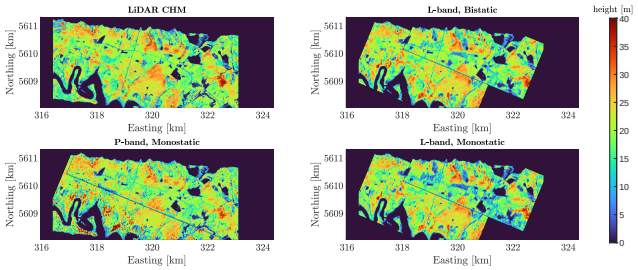

Figure 10: Comparison between LiDAR CHM map (top left) and estimated Phase Center associated to monostatic P-band (bottom left), L-band TomoSAR bistatic (top right) and monostatic (bottom right) acquisitions in NW and SE look direction

In order to have a systematic and comprehensive analysis of the performance of the estimation the model has been validated with LiDAR CHM measurements. Thus, we quantified their spatial distribution by means of a simple linear regression model defined as:

$$\boldsymbol{y} = a + b\boldsymbol{x}$$

Based on this, for each frequency band, acquisition mode and polarimetric channel, the optimal power loss value has been selected in order to minimise the bias and Root Mean Square Error (RMSE) of the distribution. Results for power loss values between 0.5 and 4 dB are shown in Fig. 11.

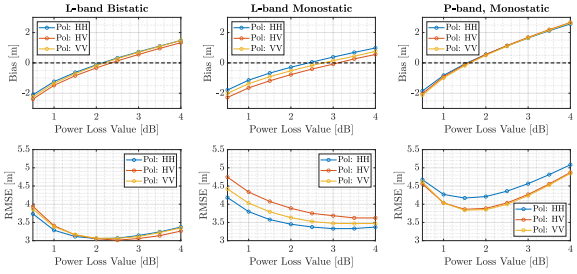

Figure 11: Canopy top height bias and RMSE versus power loss (K) with respect to the upper envelope of the phase center in the case of L-band bistatic (left), monostatic (center) and P-band monostatic TomoSAR for each polarimetric channel (HH,HV,VV).

By looking at results we select the optimal power loss value that minimise both the measure has been selected between 2.5 and 3 dB in the case of L-band bistatic and monostatic and guarantees a RMSE of about 3-3.5m, while in the case of P-band it is possible to obtain a minimum RMSE of about 3.7m with a power loss of 1.5 dB in each frequency band. Results are depicted in Fig. 12 in a 3D histogram that collect in the top panels the results associated to the estimation of the phase center, while in the bottom panels the distribution associated to the selected power loss value on the upper envelope of the phase center.

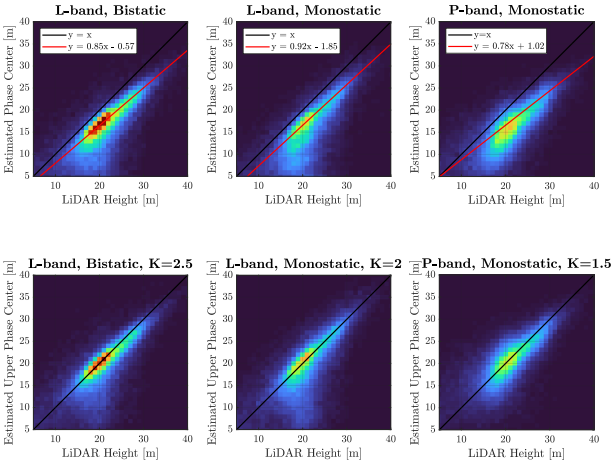

Figure 12: Correlation between Phase Centre and Upper Phase Center with respect to LiDAR CHM associated to L-band Bistatic (left panels), monostatic (center panels) and P-band monostatic (right panels), SE look at VV polarimetric channel

As can be noticed power loss values allows both to minimise the bias and increase the correlation between the measures. In addition, as can be noticed, L-band results are less sparse with respect to P-band. Finally, the refined maps are proposed in Fig. 13

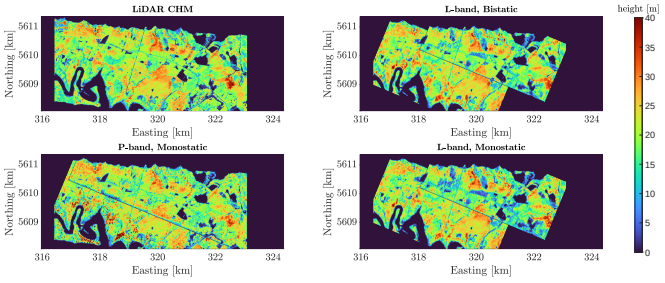

Figure 13: Comparison between LiDAR CHM map (top left) and estimated Upper Phase Center associated to monostatic P-band (bottom left), L-band TomoSAR bistatic (top right) and monostatic (bottom right) acquisitions in NW and SE look direction

6. Scientific Analysis

Kermeter forest offers a convenient landscape to investigate the effective performance of airborne TomoSAR imaging with respect to the biophysical properties associated to deciduous (beech) and conif-

erous (spruce) forests. A first discrimination between the two species can be discovered in Fig. 14 by evaluating the content of AGB and LiDAR height distributions

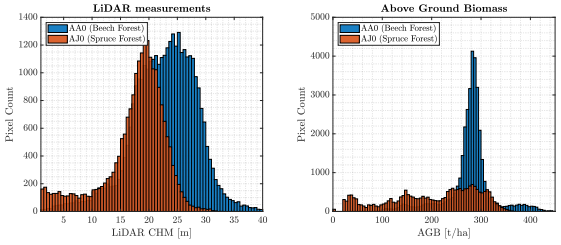

Figure 14: Histograms of the distribution of LiDAR CHM measurements (left) and Above Ground Biomass (right) considering the entire population of beeches and spruces

Table 1: Beech and Spruce Forest Characterisation

Class	Mean Forest Height	σ_h	Mean AGB	σ_{AGB}
Beech Forest	22.73 m	5.58 m	276.82 t/ha	49.36 t/ha
Spruce Forest	17.25 m	5.99 m	204.44 t/ha	88.77 t/ha

The two species shows differences both in terms of forest height, where spruces maximum height reach 30m, and AGB content suggesting that they may behave differently in TomoSAR.
In Figs. 15 and 16 the mean profiles associated to the fully polarimetric 3D TomoSAR reflectivity profiles in L-band bistatic and monostatic has been plotted in the case of beech (in blue) and spruce (in orange) trees.

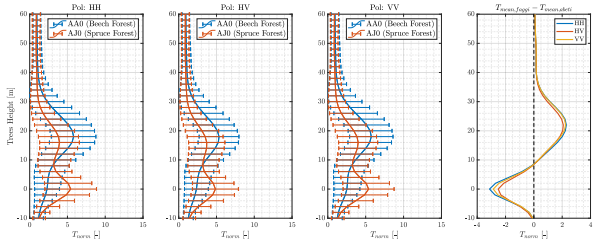

(a) L-band Bistatic

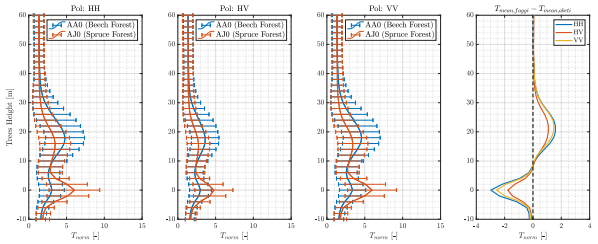

(b) L-band Monostatic

Figure 15: Mean Normalised Tomographic profiles of fully polarimetric (HH,HV,VV) L-band, SE look

Interestingly, for each L-band observation, spruces shows strong backscatter at the level of ground, while the opposite in case of beech forests. This is coherent to the mean structure of the trees: in the case of coniferous, due to the conical shape and the non thick crown, volume scattering at the level of canopy contributes less with respect to deciduous. The difference in heights between the two population of trees is reflected in the mean tomographic profiles by looking at the location of the mean phase centers which is shifted downwards in the case of spruce.

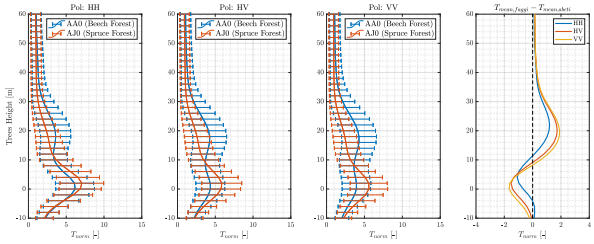

Figure 16: Mean profile of the Monostatic P-band fully polarimetric (HH,HV,VV) normalised tomograms ([0 N]) of the SE look

In Fig. 16 the mean P-band tomographic profile, differently from the L-band cases, shows spruce response at the level of ground is weaker leading to difficulties in evaluating the location of the phase center.. According to this, the following section will be focuses on assessing the correlation between TomoSAR intensities and biophysical properties of the two species to exploit the relative difference.

6.1. Relating Forest Biomass to Forest Vertical Structure

Usually, forest biomass can be directly related to the forest height by a power law defined as:

$$AGB(gr, x) = a \cdot \hat{H}(gr, x)^{\mathbf{c}} \tag{9}$$

where a and c depend on forest class and other natural conditions as stated in [18]. According to this, we may evaluate the distribution of the estimated AGB with respect to LiDAR CHM measurements and our estimated top-of-canopy height associated to P- and L-band for each forest class.
This analysis was carried in Fig. 17 by normalising the 3D histogram distribution along the column direction to evidence the the correlation features.
Results shows that the distribution of AGB and forest height is mainly driven by beech population, whose distributions follows the one found with the LiDAR measurements. On the other hand, spruces are more difficult to characterise due to the higher sparsity of the distribution. A final remark is related to P-band performances which are coarser with respect to L-band to investigate the relation between AGB and canopy height.

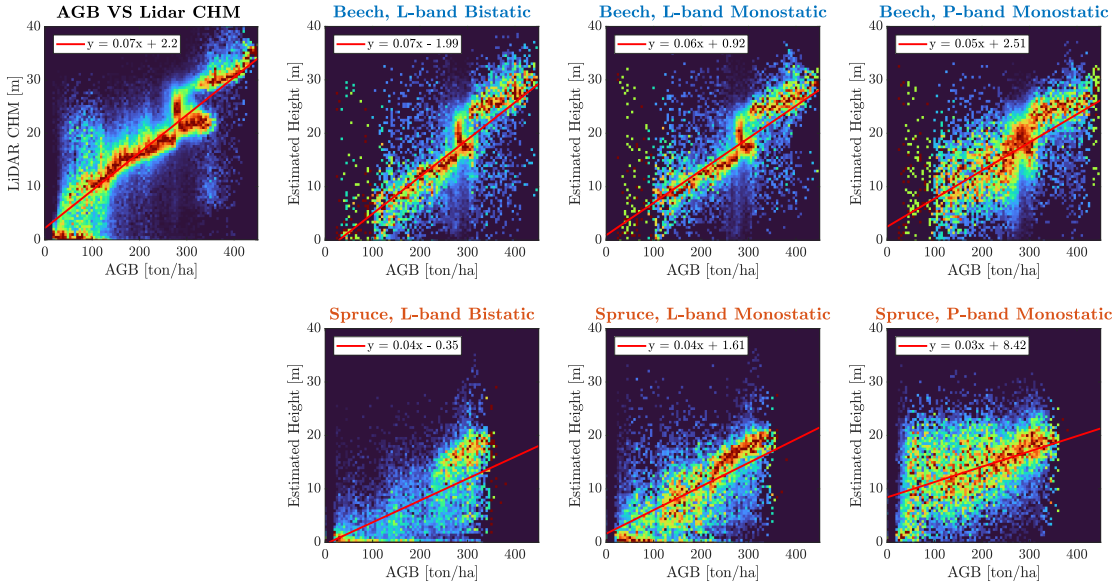

Figure 17: Correlation between Above Ground Biomass and Lidar CHM (top left), estimated top-of height canopy in the case of L-band bistatic, L-band monostatic and P-band at VV Polarimetric channel, by separating the contribution of Spruce and Beech Forests

6.2. Relating Forest Biomass to SAR Tomography

In Fig. 18 the fully polarimetric distribution of AGB and RVoG are plotted according to each frequency band. The results in L-band shows linear trends both in the case of Spruce and Beech with an increased correlation in case of bistatic where the canopy contribution is more coherent with respect to the mostatic mode. In the case of P-band, instead, a difference in the relative distribution of spruce and beech can be found. Thus, spruce forest's shows complete uncorrelation, while in the case of beech a linear dependency can be still found. These are promising results, confirming that radar sensors are sensible to

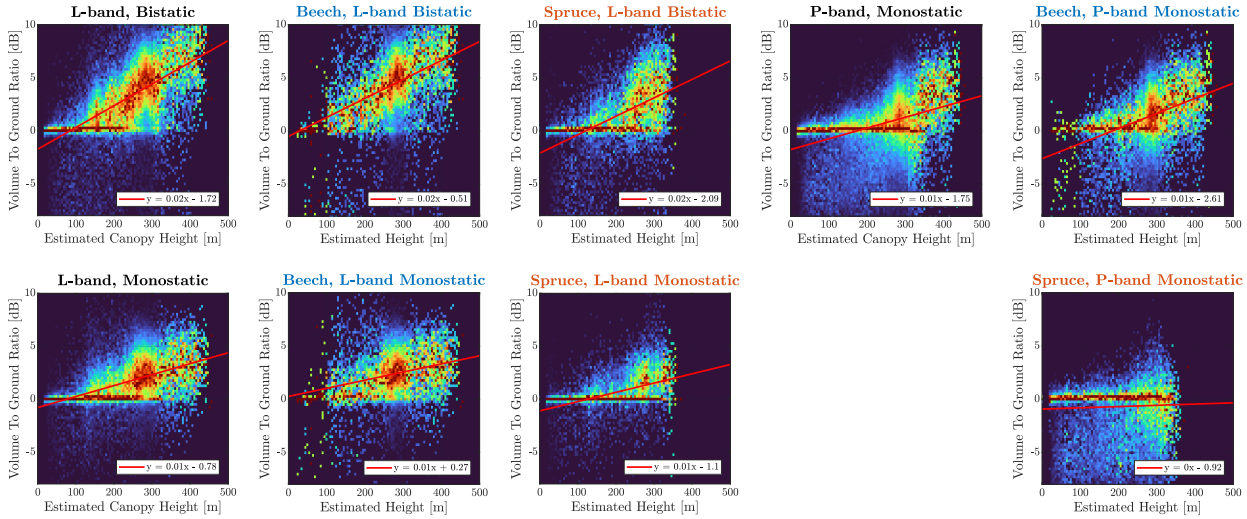

Figure 18: Correlation between Above Ground Biomass and Volume To Ground Ratio in the case of L-band bistatic, L-band monostatic and P-band at VV Polarimetric channel, by separating the contribution of entire forest (titles in black), spruce (titles in orange) and beech (titles in blue)

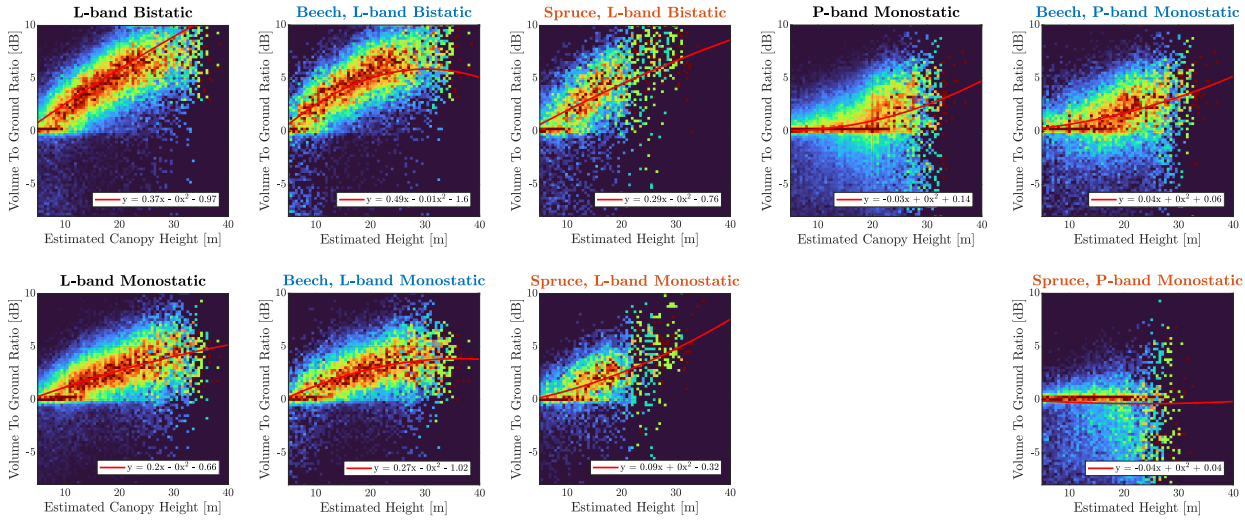

Figure 19: Correlation between Estimated Canopy Height and Volume To Ground Ratio in the case of L-band bistatic, L-band monostatic and P-band at VV Polarimetric channel, by separating the contribution of entire forest (titles in black), spruce (titles in orange) and Beech (titles in blue) Forests

the dielectric constant of the scene and can describe, partially, the contribution associated to biophysical parameters, such as the biomass.

6.3. Relating Canopy Height to SAR Tomography

Finally this section propose the analysis on the dependency between TomoSAR intensities and forest biomass. The results are illustrated in Fig. 5 where titles in black indicates analysis on the entire ROI, while in blue and organge the analysis on beech and spruce respectively. The distributions shows almost a quadratic dependency modeled as:

$$\boldsymbol{y} = a + b\boldsymbol{x} + c\boldsymbol{x}.^{\mathbf{2}} \tag{10}$$

P-band shows spruces distribution completely uncorrelated, while poorly correlated in case of beech forest for heigth above 20m. In the case of L-band it is possible to underline two main difference between monostatic and bistatic acquisitions:

- Higher correlation in L-band bistatic
- Different concavity between deciduous and coniferous distributions

The first can be justified by the higher coherences exhibits by bistatic acquisition, while the second requires additional analysis. Interestingly, RVoG tends to decrease for forest heights that exceed the mean forest heights in the case of spruces. This may be explained by analysing the principal scattering mechanism that occurs in forest SAR imaging:

1. Direct Terrain Backscattering
2. Volume Scattering
3. Double Bounce scattering from trunk-ground interaction
4. Double Bounce scattering from canopy-ground interaction

While the first contribution is almost independent on the height of the forest, the latter can be strongly affected by the trees parameters (e.g. canopy height, shape, etc..). Thus, the decreasing trend may be explained by double bounce phenomenon that can scatter far away the signal in case of increasing height, while the difference between spruces and beech woods, may be strongly influenced by the evident difference in trees shape.

7. Conclusions

This thesis has investigated the benefits and potentiality that arise from the utilization of low frequency band Synthetic Aperture Radar Tomography in Forest Remote Sensing. As the link between biophysical forest structure and the reconstructed 3D radar reflectivity is still not understood and is far from being completely established, the 3D radar profiles obtained open prospects to derive algorithms that are able to link these profiles to the physical structure of the forest. For future work, we aim to provide one of the potential directions of one of the most complete SAR dataset ever collected. Together, the results obtained in the context of this thesis demonstrate the potentiality of P- and L-band SAR Tomography. L-band has demonstrated higher sensitivity in mapping and characterising the forest structure and this can represent an interesting results that reinforce the scientific basis for the investigation and monitoring of forests for future SAR mission.

References

[1] Ian J Wright, Ning Dong, Vincent Maire, I Colin Prentice, Mark Westoby, Sandra Díaz, Rachael V Gallagher, Bonnie F Jacobs, Robert Kooyman, Elizabeth A Law, et al. Global climatic drivers of leaf size. *Science*, 357(6354): 917–921, 2017.

[2] Yude Pan, Richard A. Birdsey, Jingyun Fang, Richard Houghton, Pekka E. Kauppi, Werner A. Kurz, Oliver L. Phillips, Anatoly Shvidenko, Simon L. Lewis, Josep G. Canadell, Philippe Ciais, Robert B. Jackson, Stephen W. Pacala, A. David McGuire, Shilong Piao, Aapo Rautiainen, Stephen Sitch, and Daniel Hayes. A large and persistent carbon sink in the world’s forests. *Science*, 333(6045): 988–993, 2011.

[3] S. Tebaldini, Dinh Ho Tong Minh, M. Mariotti d'Alessandro, Ludovic Villard, Thuy Le Toan, and J. Chave. The status of technologies to measure forest biomass and structural properties: state of the art in SAR tomography of tropical forests. *Surveys in Geophysics*, 40(4):779–801, 2019. doi: 10.1007/s10712-019-09539-7. URL https://hal.inrae.fr/hal-02609702.

[4] Maciej J. Soja, Shaun Quegan, Mauro M. d'Alessandro, Francesco Banda, Klaus Scipal, Stefano Tebaldini, and Lars M.H. Ulander. Mapping above-ground biomass in tropical forests with ground-cancelled p-band sar and limited reference data. *Remote Sensing of Environment*, 253:112153, 2021. ISSN 0034-4257. doi: https://doi.org/10.1016/j.rse.2020.112153. URL https://www.sciencedirect.com/science/article/pii/S0034425720305265.

[5] Mauro Mariotti d'Alessandro, Stefano Tebaldini, and Fabio Rocca. Phenomenology of ground scattering in a tropical forest through polarimetric synthetic aperture radar tomography. *IEEE Transactions on Geoscience and Remote Sensing*, 51(8):4430–4437, 2013. doi: 10.1109/TGRS.2013.2246573.

[6] Stefano Tebaldini and Fabio Rocca. Multibaseline polarimetric sar tomography of a boreal forest at p- and l-bands. *IEEE Transactions on Geoscience and Remote Sensing*, 50(1):232–246, 2012. doi: 10.1109/TGRS.2011.2159614.

[7] Shaun Quegan, Thuy Le Toan, Jerome Chave, Jorgen Dall, Jean-François Exbrayat, Dinh Ho Tong Minh, Mark Lomas, Mauro Mariotti D'Alessandro, Philippe Paillou, Kostas Papathanassiou, Fabio Rocca, Sassan Saatchi, Klaus Scipal, Hank Shugart, T. Luke Smallman, Maciej J. Soja, Stefano Tebaldini, Lars Ulander, Ludovic Villard, and Mathew Williams. The european space agency biomass mission: Measuring forest above-ground biomass from space. *Remote Sensing of Environment*, 227:44–60, 2019. ISSN 0034-4257. doi: 10.1016/j.rse.2019.03.032.

[8] Stefano Tebaldini, Mauro Dalessandro, L.M.H. Ulander, Anders Gustavsson, Alex Coccia, Karlus Camara de Macedo, Mathias Disney, Hans-Joachim Spors, Nico Schumacher, Jan Hanus, Jan Novotny, Dirk Schuettemeyer, and Klaus Scipal. The tomosense experiment: Mono- and bistatic sar tomography of forested areas at p-, l-, and c-band. pages 7955–7958, 07 2021. doi: 10.1109/IGARSS47720.2021.9553043.

[9] Alberto Moreira, Gerhard Krieger, I. Hajnsek, Konstantinos Papathanassiou, Marwan Younis, Paco Lopez Dekker, Sigurd Huber, Michael Eineder, Masanobu Shimada, Takeshi Motohka, Manabu Watanabe, Masato Ohki, Akihisa Uematsu, and Satoru Ozawa. Tandem-l: A highly innovative bistatic sar mission for global observation of dynamic processes on the earth's surface. volume 3, 06 2015. doi: 10.1109/MGRS.2015.2437353.

[10] Christian Barbier, Dominique Derauw, Anne Orban, and Malcolm W. J. Davidson. Study of a passive companion microsatellite to the SAOCOM-1B satellite of Argentina, for bistatic and interferometric SAR applications. In Roland Meynart, Steven P. Neeck, and Haruhisa Shimoda, editors, *Sensors, Systems, and Next-Generation Satellites XVIII*, volume 9241, pages 139 – 150. International Society for Optics and Photonics, SPIE, 2014. doi: 10.1117/12.2066307. URL https://doi.org/10.1117/12.2066307.

[11] Bastian Siegmann, Luis Alonso, Marco Celesti, Sergio Cogliati, Roberto Colombo, Alexander Damm, Sarah Douglas, Luis Guanter, Jan Hanuš, Kari Kataja, Thorsten Kraska, Maria Matveeva, Jóse Moreno, Onno Muller, Miroslav Pikl, Francisco Pinto, Juan Quirós Vargas, Patrick Rademske, Fernando Rodriguez-Morene, Neus Sabater, Anke Schickling, Dirk Schüttemeyer, František Zemek, and Uwe Rascher. The high-performance airborne imaging spectrometer hyplant—from raw images to top-of-canopy reflectance and fluorescence products: Introduction of an automatized processing chain. *Remote Sensing*, 11(23), 2019. ISSN 2072-4292. doi: 10.3390/rs11232760. URL https://www.mdpi.com/2072-4292/11/23/2760.

[12] Mauro Mariotti d'Alessandro, Yanghai Yu, Stefano Tebaldini, and Mingsheng Liao. Tomo-

graphic calibration of the new esa tomosense campaign. pages 3089–3092, 07 2021. doi: 10.1109/IGARSS47720.2021.9553873.

[13] Richard Bamler and Ph. Hartl. Synthetic aperture radar interferometry. *Inverse Problems*, 14, 1998.

[14] S. Tebaldini and Laurent Ferro-Famil. SAR tomography from bistatic single-pass interferometers. In *37th Annual IEEE International Geoscience and Remote Sensing Symposium, IGARSS 2017*, volume 2017-July, pages 133–136, Fort Worth, United States, July 2017. Institute of Electrical and Electronics Engineers Inc. doi: 10.1109/IGARSS.2017.8126912. URL https://hal-univ-rennes1.archives-ouvertes.fr/hal-01739939.

[15] Matteo Pardini, Andrea Cantini, Fabrizio Lombardini, and Konstantinos Papathanassiou. 3-d structure of forests: First analysis of tomogram changes due to weather and seasonal effects at l-band. In *EUSAR 2014; 10th European Conference on Synthetic Aperture Radar*, pages 1–4, 2014.

[16] Stefano Tebaldini and Fabio Rocca. Multibaseline polarimetric sar tomography of a boreal forest at p- and l-bands. *IEEE T. Geoscience and Remote Sensing*, 50:232–246, 01 2012. doi: 10.1109/TGRS.2011.2159614.

[17] Dinh Ho Tong Minh, Thuy Le Toan, Fabio Rocca, Stefano Tebaldini, Ludovic Villard, Maxime Réjou-Méchain, Oliver L. Phillips, Ted R. Feldpausch, Pascale Dubois-Fernandez, Klaus Scipal, and Jérôme Chave. Sar tomography for the retrieval of forest biomass and height: Cross-validation at two tropical forest sites in french guiana. *Remote Sensing of Environment*, 175:138–147, 2016. ISSN 0034-4257. doi: https://doi.org/10.1016/j.rse.2015.12.037. URL https://www.sciencedirect.com/science/article/pii/S0034425715302595.

[18] I.H. Woodhouse. Introduction to microwave remote sensing. *CRC Press*, 2006. doi: 10.1201/9781315272573. URL https://doi.org/10.1201/9781315272573.